Materials and Design 137 (2018) 204–213

Contents lists available at ScienceDirect

Materials and Design

journal homepage: www.elsevier.com/locate/matdes

Micromechanics modeling of metallic alloys 3D printed by selective laser melting

Mohsen Taheri Andani [a], Mohammad Reza Karamooz-Ravari [b], Reza Mirzaeifar [c], Jun Ni [a,*]

[a] S.M. Wu Manufacturing Research Center, College of Engineering, Department of Mechanical Engineering, University of Michigan, Ann Arbor, MI 48109, USA
[b] Department of Mechanical Engineering, Graduate University of Advanced Technology, Kerman, Iran
[c] Department of Mechanical Engineering, Virginia Tech, Blacksburg, VA 24061, USA

HIGHLIGHTS

- Developing a novel method to generate actual micro structures of SLM components
- Developing a computational model for predicting the mechanical response of SLM materials
- Capturing the effect of processing defects on mechanical properties of SLM materials

GRAPHICAL ABSTRACT

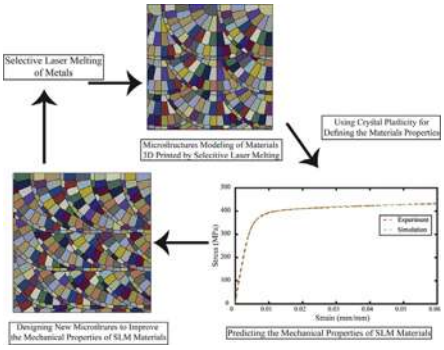

ARTICLE INFO

Article history:
Received 21 August 2017
Received in revised form 4 October 2017
Accepted 8 October 2017
Available online 10 October 2017

Keywords:
Selective laser melting
3D printing
Micromechanics
Crystal plasticity
Stainless steel
Materials modeling

ABSTRACT

Nowadays, additive manufacturing of metallic materials plays a key role in manufacturing technology due to its unique capability of printing strong and complicated components with high precision. Currently, the approach to obtain a specific mechanical performance in 2D printed metallic parts is a challenging and expensive iterative process. Using computational models to predict the mechanical properties of selective laser melting (SLM) metallic alloys based on their microscopic features can be leveraged to reduce the iteration cost for obtaining the desired mechanical properties. An accurate computational model will also be a superior tool to investigate practical modifications in the processing parameters to improve the mechanical performance of 3D printed metals. In this paper, a novel technique is developed to study the correlation between microstructural features, including melt pools and grain structures, and the macroscopic mechanical properties of SLM products. Crystal plasticity is utilized and calibrated to represent the material properties of grains. The capability of the model in considering the role of texture, process defects, mechanical loading direction, and laser scan hatch space on the mechanical behavior of SLM parts are evaluated. The good agreement between the obtained results and the reported experimental data confirms the accuracy of the developed computational model.

1. Introduction

Selective laser melting (SLM), as a novel additive manufacturing (AM) method, has been considered as a promising future in the next industrial revolution [1]. In this manufacturing process, the object is

* Corresponding author at: 3455 GGB (George G. Brown Laboratory), 2350 Hayward, Ann Arbor, MI 48109, USA.
E-mail addresses: mtaheri@umich.edu (M. Taheri Andani), m.karamooz@kgut.ac.ir (M.R. Karamooz-Ravari), rmirzaei@vt.edu (R. Mirzaeifar), junni@umich.edu (J. Ni).

https://doi.org/10.1016/j.matdes.2017.10.026
0264-1275/

Table 1
Process parameters and the resulting energy input used in this study.

Effective laser power W	Layer thickness μm	Scan velocity mm/s	Hatch space μm	Energy input J/mm^3
200	30	800	120	69.4

designed in three-dimension (3D) using a computer-aided design (CAD) software and then is fabricated layer-by-layer by selectively melting of powders [2]. Consequently, SLM process shows a great advantage of design flexibility, which enables the fabrication of parts with extremely complicated morphologies compared to conventional manufacturing processes such as casting and forging [2,3]. With the advancement of selective laser melting process, the modeling and simulation have gained extensive attention during the last few years. Modeling and simulation advance our capability from designing novel structure (macro scale) to controlling the microstructure of the components (mesoscale) to meet the required performance [4]. It can also help to quantify the effect of process variables on resulting functional properties of components [5–10]. Consequently, it enhances the current trial and error approaches in the optimization of microstructural and functional properties of SLM products.

Current studies on modeling and simulation are mostly focused on simulating the laser processing at multiple length scales. For example, Foroozmehr et al. [11] simulated the solidification process during SLM at the macro scale. Prediction of melt pool geometry and the induced residual stresses in the final products are the main outputs of their works. Khairallah et al. [12] and Panwisawas et al. [13] developed a novel technique to simulate the SLM manufacturing process at the powder scale level. Their works capture the details of laser interaction with the powder, including vaporization effect, which can lead to a determination of spattering and denudation during laser processing. They also took the temperature and time histories of the melt pool into account which might be used to determine surface finish and part density.

Moreover, some limited works are devoted to simulating the solidification process during additive manufacturing of metallic alloys. Acharya et al. [14] used computational fluid dynamics (CFD) analysis to predict melt pool characteristics and phase field modeling to simulate microstructure evolution in the as-deposited state for SLM process. Various microstructure features such as segregation of secondary elements, dendrite sizes, dendritic orientation, and surface roughness are assessed and validated through comparison with experimental data. In another similar work, Nie et al. [15] developed a multiscale model to simulate the evolution of the microstructure of a Nb-bearing nickel-based superalloy during laser additive manufacturing solidification. The model predicts the nucleation and growth of dendrites, the segregation of niobium (Nb), and the formation of Laves phase particles during the solidification. This provides the relationship between the solidification conditions and the resultant microstructure.

Despite all the studies on modeling and simulation of SLM process, our fundamental understanding of the material behavior at macro scale, considering the microstructural properties, is still highly limited. The presence of melt pools, besides the grains and grain boundaries, increase the microstructural complexities of the SLM products which consequently complicates connecting the microstructural features to the macroscopic mechanical response of the manufactured SLM materials. In this work, a novel computational framework is developed to accurately predict the mechanical response of SLM processed materials, considering the geometrical features of both the grains and melt pools explicitly in the material. First, the explicit microstructural representation (morphology and crystallographic orientations of grains and melt pools) of a 316L stainless steel component is created in a finite element model (FEM). Physically based crystal plasticity (CP) constitutive model is then implemented into the model to define the material properties of the bulk grains and melt pools. The FEM model is calibrated and validated using experimental data obtained by uniaxial tension tests of 316 L stainless steel samples. Several finite element models are simulated to assess the effects of level of porosity, melt pool size, crystallographic textures of grains, and loading conditions on the mechanical response of SLM products. This work provides a step toward an integrated computational materials engineering (ICME) approach, where models of SLM materials processes are bridged to ones of properties.

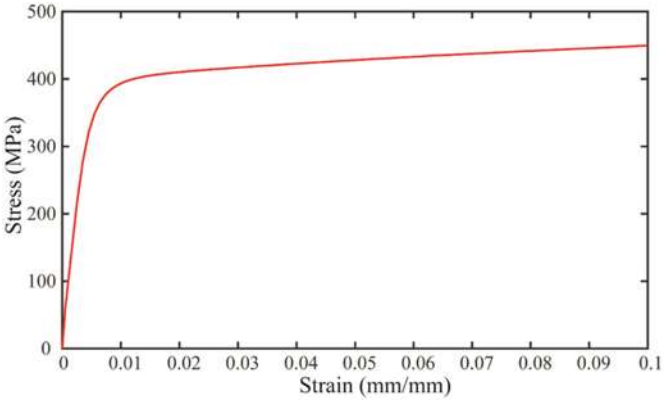

Fig. 2. The tensile stress-strain response of the polycrystalline SLM 316L stainless steel up to 10% of strain. This curve is used to calibrate the crystal plasticity material parameters in this study.

2. Materials and methods

An SLM 280HL (SLM Solutions Inc., Lübeck Germany) machine equipped with two 400 W CW Ytterbium fiber lasers beams is used to fabricate specimens. The laser beams have diameters of approximately 80 μm at the focal point of laser radiation. The building platform of the machine has dimensions of 280 × 280 × 350 mm. Argon gas is flooded into its chamber to reduce the oxygen level to <0.1% before the operation. The pre-alloyed 316 L stainless steel powder, which has been gas atomized, is used as printing powder. The average particle size is

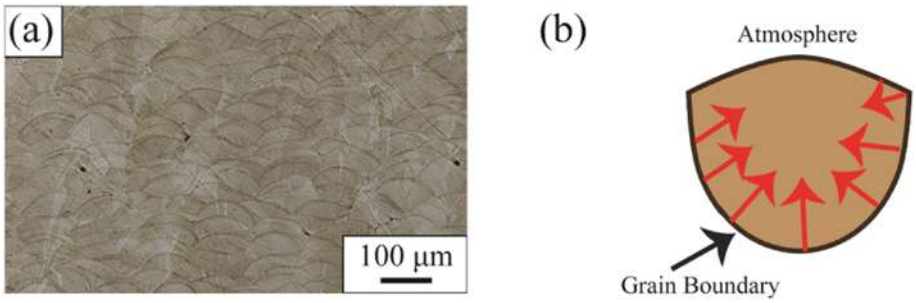

Fig. 1. (a) The optical microscopy image of a cross-section perpendicular to the laser beam direction of an SLM 316L stainless steel sample. (b) A schematic representation of one melt pool. Red arrows show the growth orientation of columnar grains in the melt pool. (For interpretation of the references to color in this figure legend, the reader is referred to the web version of this article.)

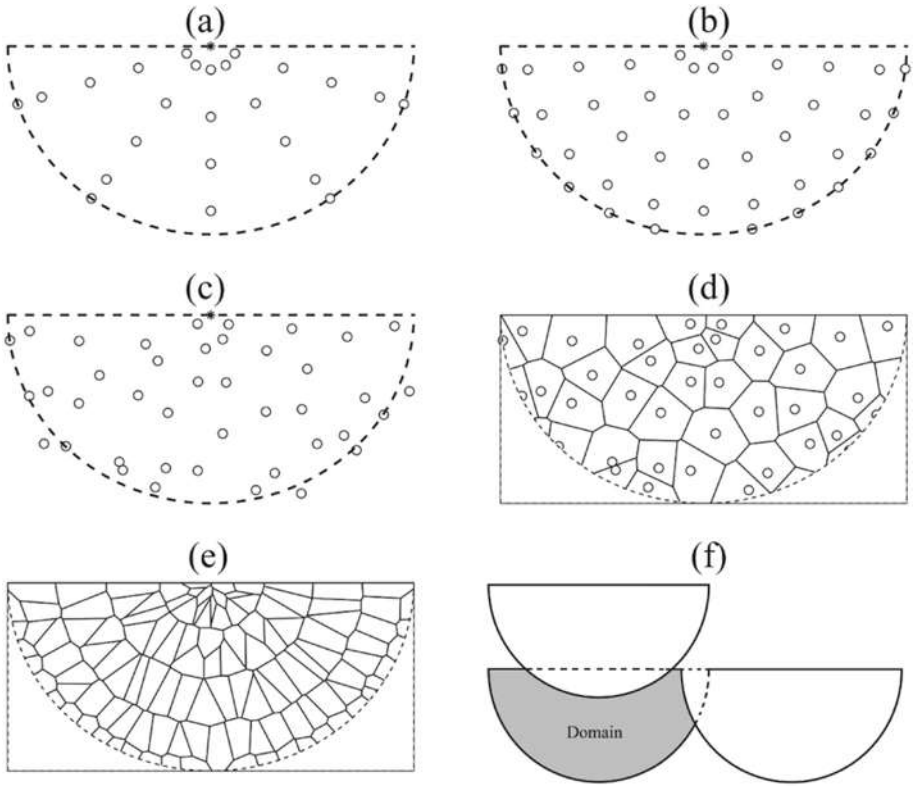

Fig. 3. (a) 2D representation of regularly distributed initial points in a semi-circle for $n_r = n_\theta = 4$, and $n_z = 1$. (b) Regularly distributed initial points considering the number of circumferential points varies as a linear function of the radius. (c) Regularly distributed initial points in a semi-circle domain. (d) 2D schematic Voronoi tessellation of a semi-circle using $n_r = 4$, $n_\theta^1 = 4$, $n_\theta^2 = 12$, and $L_r = L_\theta = 0.5$. (e) A columnar Voronoi tessellation using $n_r = 4$, $n_\theta^1 = 15$, and $n_\theta^2 = 30$. (f) A truncated melt pool and its corresponding domain.

ranging between 30 μm and 50 μm. Dense cuboid 10 × 6 × 10 mm samples and tensile specimens in accordance with the ASTM/E8 standard [16] are fabricated for microscopic analysis and mechanical testing, respectively. Process parameters listed in Table 1 are utilized to fabricate fully dense parts. In this table, the energy input is calculated using the following relation [17]:

$$E = \frac{P}{v.h.t} \tag{1}$$

where P, v, h, and t are laser power (W), laser scanning speed (mm/s), hatch spacing (mm), and layer thickness (mm), respectively.

In order to simplify the geometry of representative volume elements (RVE) used in finite element modeling, the bi-directional scanning strategy, at which the laser moves across each layer in a zigzag pattern, is used to fabricate the samples.

Microscopy analysis is performed by optical microscopy (Leica DM4000M). Cuboid samples are polished through diamond suspensions of 9 μm, 6 μm, and 3 μm and finally, alumina suspensions of 1 μm and 0.05 μm to result in a smooth surface. Tension tests are performed by

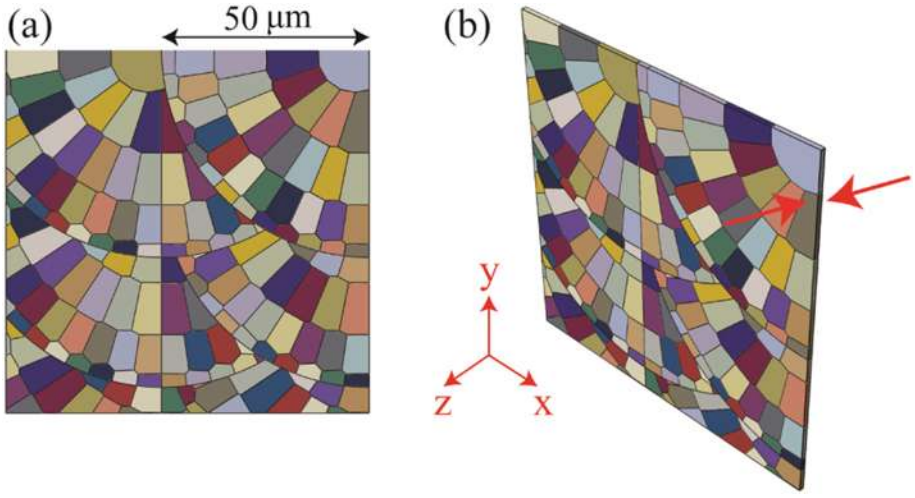

Fig. 4. (a) 2D RVE representing the microstructural features of SLM components, (b) 3D RVE with a semi-plane stress condition. To decrease the cost of the analysis and complexity of 3D RVE, a semi-plane stress condition RVE is simulated in this study. The red arrows show the very small thickness in depth of the model. (For interpretation of the references to color in this figure legend, the reader is referred to the web version of this article.)

Table 2
Boundary Conditions applied to the RVE model (a × a × thickness).

Model face	Boundary condition	
Top (y = a)	v = displacement;	$t_1 = t_3 = 0$
Bottom (y = 0)	$v = 0$;	$t_1 = t_3 = 0$
Left (x = 0)	$u = -\overline{u}_1$	$t_2 = t_3 = 0$
Right (x = a)	$u = \overline{u}_1$;	$t_2 = t_3 = 0$

the 150 kN INSTRON machine at a strain rate of $10^{-4}\ s^{-1}$. The strain is measured by an EPSILON extensometer with a gauge length of 25 mm which is attached to the samples. Tensile tests are repeated three times and their average response is plotted.

3. Microstructure and tensile behavior of SLM 316L stainless steel

Fig. 1(a) shows the optical microscopy image of a cross-section perpendicular to the laser beam direction of an SLM 316L stainless steel sample. The melt pools have arc-shaped configuration attributed to the Gaussian energy distribution of the laser beam. Melt pool boundaries are generated through overlapping the layers in building and laser scan directions. A schematic of the cross-section of one molten pool is illustrated in Fig. 1(b), the upper half of the liquid molten pools are in conjunction with atmosphere and consequently the heat flux transfers in a radiation manner. The melt pool boundaries are in touch with the solidified metal layer or substrate, in which the heat flux transfers in a conduction mode. Similar to the casting processes, a non-homogenous nucleation on the solid phase boundary (grain boundary) of each melt pool is created and epitaxial grains are induced. Subsequently, new nucleated grains are created and grow further toward the center of the melt pools. The red arrows show the growth orientation of these columnar grains in Fig. 1(b).

Fig. 2 shows the experimentally obtained tensile stress-strain response of the SLM 316L stainless steel sample up to 10% of strain. The elastic behavior, level of yield strength (~400 MPa), and the plastic flow are in good agreement with the previously reported works [18]. The existing small differences are due to the selection of bi-directional laser scan strategy as explained in Section 2.

4. Mesoscale modeling of SLM 316L

4.1. Grain-scale modeling based on Voronoi tessellation

Voronoi tessellation technique is widely accepted to represent polycrystalline aggregates as it provides a realistic approximation of the microstructure of non-uniform grain shapes [19,20]. Voronoi cells are constructed from a series of randomly positioned points (generators) in the given domain. Each Voronoi cell, representing the one-grain structure, is the set of all points in the given domain whose distances from the corresponding generator are not greater than their distances from the other generators.

In order to construct a Voronoi tessellated domain, it is necessary to generate some initial points in the desired domain as generators. The way one generates the initial points determines the final shape of the Voronoi cells of the domain. In this paper, the distribution of the initial points is performed according to the real microstructure of the material. To do so, it is assumed that the melt pools are semi-cylinders which may be oriented around the axis normal to the building platform. Accordingly, in order to construct each melt pool, some initial points might be distributed in a semi-cylinder in three dimensions or in a semi-circle in two dimensions. The regularly distributed points may be generated in a polar coordinate system using the following equation:

$$\begin{Bmatrix} r \\ \theta \\ z \end{Bmatrix}_i = \begin{Bmatrix} \frac{R_m}{n_r}\left(i-\frac{1}{2}\right) \\ \frac{\pi}{n_\theta}\left(i-\frac{1}{2}\right) \\ \frac{L_m}{n_z}\left(i-\frac{1}{2}\right) \end{Bmatrix} \tag{2}$$

in which r, θ, and z are respectively the radial, tangential, and axial coordinates of the i-th point in cylinderical coordinate system, n_r, n_θ, and n_z are the number of points in the r, θ, and z directions correspondingly. R_m is the radius of the melt pool, and L_m is the length of the sample along the melt pool. Fig. 3(a) shows a 2D representation of regularly distributed initial points in a semi-circle by setting $n_r = n_\theta = 4$, and $n_z = 1$.

As it can be seen, the distance between circumferential points varies by the radius at which the points are located. This distance is larger for the points far from the center of the circle. It causes the size of the Voronoi cells, which would be the grains of the material, gets bigger by getting far from the center of the circle. Accordingly, the size of the grains would really vary throughout one single melt pool without any control over them, that is really far from what is observed in reality. To compel this difficulty, it is supposed that the number of circumferential points is changed as a function of radius using the following equation:

$$n_\theta = int\left(n_\theta^1 + \frac{n_\theta^2 - n_\theta^1}{\frac{R_m}{n_r}(n_r - 1)}\left(r - \frac{R_m}{2n_r}\right)\right) \tag{3}$$

where r is the radius at which the points are going to be located, n_θ^1 and n_θ^2 are the number of the circumferential points at $r(i=1)$ and $r(i=n_r)$, respectively, and int(·) is a fuction which converts a real number to an integer. This equation means the number of circumferential points varies as a linear function of the radius. Fig. 3(b) shows the regularly distributed initial points produced using the above-mentioned approach with $n_r = 4$, $n_\theta^1 = 4$, $n_\theta^2 = 12$, and $n_z = 1$. Since the grians in the microstructure of a material are randomly distributed, it is inevitable that the Voronoi tessellation of the desired domain is performed randomly. To do so, one can generate the initial points randomly which cause the shape of the cells of the Voronoi tessellation and their distribution be random too. In this paper, the randomly distributed initial points are generated by moving the points of the regularly distributed initial points to a random position within a spherical domain (in the case of 2D problems the domain would be a circle) using the following equations:

$$\begin{Bmatrix} r \\ \theta \\ z \end{Bmatrix}_i^{rand} = \begin{Bmatrix} r \\ \theta \\ z \end{Bmatrix}_i^{reg} + \begin{Bmatrix} \frac{R_m}{2n_r}\alpha_r L_r \\ \frac{\pi}{2n_\theta}\alpha_\theta L_\theta \\ \frac{L_m}{2n_z}\alpha_z L_z \end{Bmatrix} \tag{4}$$

in which the upper cases “rand” and “reg” indicate the randomly and regularly distributed initial points. α_r, α_θ, and α_z are random real

Table 3
Geometrical feature of RVEs which studied in this work to identify the proper RVE size.

RVE number	Number of grains	Number of melt pools	Number of elements
1	32	2	2847
2	93	4	6901
3	188	6	12,417
4	222	9	14,357
5	319	11	20,085
6	457	16	28,419
7	653	20	39,896

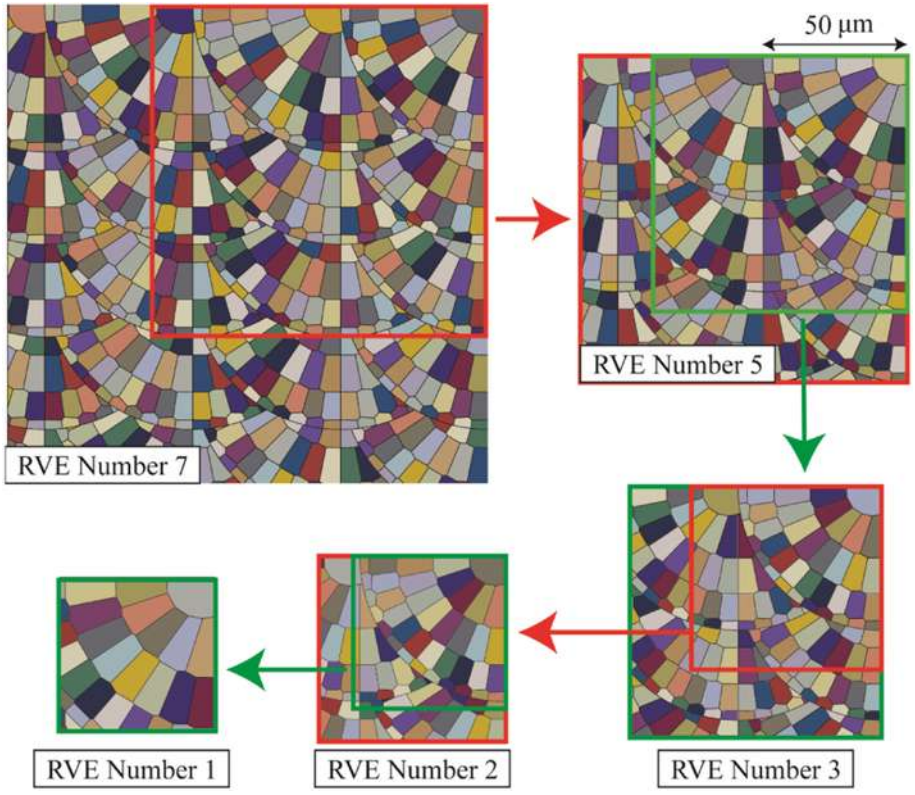

Fig. 5. Schematic representatives of RVEs used to determine the proper RVE size. The number of melting pools and the grains are decreased from RVE number 7 to RVE number 1 as shown in the figure.

numbers between −1 and 1, and L_r, L_θ, and L_z are real numbers between 0 and 1 which indicate the level of randomness for radial, tangential, and axial directions correspondingly. For the level of randomness of 0, the points would be distributed regularly while the highest level of randomness would be happened if these parameters set as 1. Fig. 3(c) shows 2D randomly distributed points using $L_r = L_\theta = 0.5$. When the random distribution approach is utilized, the distance between two neighbor points would get to small. It leads to the creation of very small Voronoi cells which may cause some problems in meshing the final part. To compel this problem, after creation of each random initial point, its distance to all the other existing initial points is checked. If the distance to at least one of the other points is smaller than a criterion, ε, that point will be ignored for the tessellation of the space.

After generation of the initial points, it is time to tessellate the domain of interest. In this paper, the Python program named as PYVORO developed by Rycroft [21] is used for tessellation of the space. The input of the code is a set of initial points and its output is a set of cells associated with each point. Each cell in this set consists of a set of faces (or lines in the case of 2D space) and each face (line) consists of a set of vertices and their connections. These data are then utilized for the construction of the finite element model of each melt pool through a python script for ABAQUS 6.13-4 package. Fig. 3(d) shows the 2D

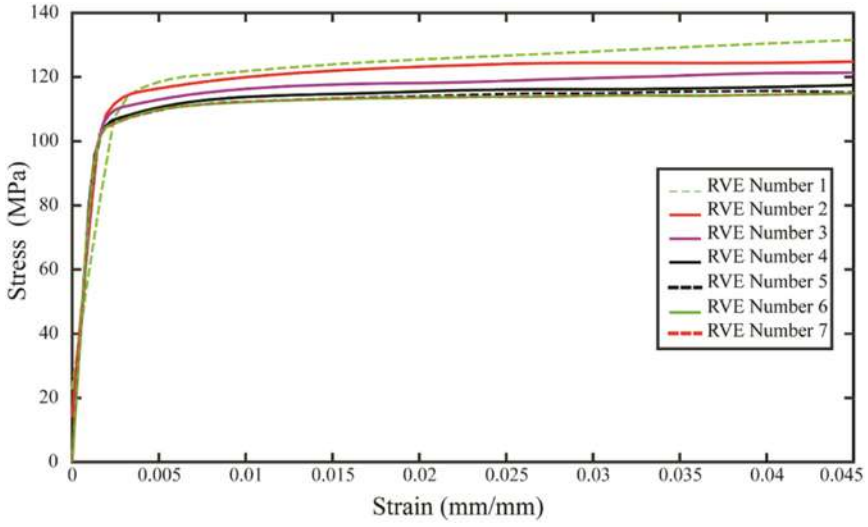

Fig. 6. Stress (along y-axis)-strain (along y-axis) response of different RVEs size under similar loading conditions. The results converge to an effective value for the RVEs larger than RVE number 4. In this work, RVE number 5 is selected as the proper RVE size which can objectively reflect the macroscopic features of SLM components.

schematic of a random Voronoi tessellation of a semi-circle. The SEM images demonstrate that the grains of an additively manufactured part is almost columnar [22–24]. To construct a model similar to what the real microstructure is, the Voronoi cells must be columnar too. It can be obtained by setting appropriate values for the parameters of the Voronoi tessellation scheme including n_r, n_θ^1, and n_θ^2. A nearly columnar Voronoi tessellation using $n_r = 4$, $n_\theta^1 = 15$, and $n_\theta^2 = 30$ is shown in Fig. 3(e). The above-mentioned approach is performed for each melt pool separately. Then, the total representative volume element (RVE) is produced by assembling all the melt pools together. It must be noticed that the boundaries of a melt pool might be different from a complete semi-cylinder due to the truncation by the neighbor melt pools as shown in Fig. 3(f). If it happens, the Voronoi tessellation must be applied to the truncated semi-cylinder (the gray domain in Fig. 3(f) instead.

4.2. Extension of the 2D RVE to a 3D RVE with a semi-plane stress condition

To investigate the effect of stress state on the mechanical properties in the micromechanical modeling of SLM materials, loadings under different stress conditions should be studied. Complex stress conditions can be generated by applying boundary conditions (BCs) in a cubic 3D RVE model. Nevertheless, the seeding and tessellation approaches described in Section 4.1 become much more complicated for 3D cases. Moreover, the number of elements and grains structures increase significantly and the computational efficiency drops accordingly. To overcome the shortcomings of the conventional 3D model, the 3D model with a very small thickness in depth (similar to the plane stress conditions) are studied in this work as a compromise (Fig. 4). Similar to the plane stress condition, the stress in the depth direction could be neglected in this work. Consequently, the results compared to 3D RVEs are conservative. This is why the focus of future work should be on conducting more realistic and accurate 3D simulations. More information on semi-plane stress condition can be found in [25,26].

Mechanical periodic boundary conditions as described in Table 2 [27] are applied to the computational domain. In this table, t_1, t_2, and t_3 represent the tractions in X,Y, and Z directions, respectively. Also, $\overline{u}_1$ represents the displacement of the right/left face in the x direction upon loading on the top surface. The stress- strain values reported in this study are engineering values. The stress is defined as the forced divided by the undeformed cross-section area of the top surface.

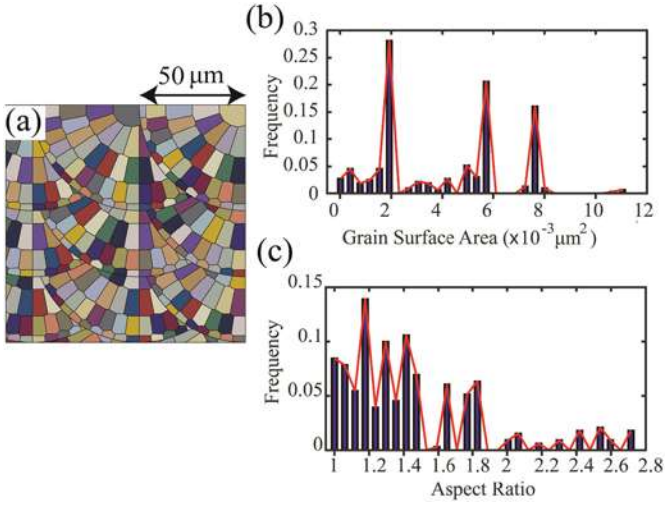

Fig. 7. (a) Schematic representative of the proper RVE size determined for micromechanics modeling in this work. (b) The surface distribution of the grains in the chosen RVE. (c) The aspect ratio distribution of grains in the selected RVE.

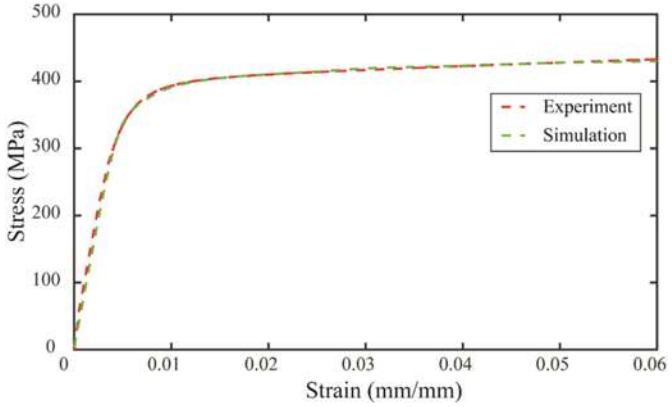

Fig. 8. The comparison of experimental data and simulation results using the calibrated materials constants. A good agreement can be observed.

4.3. Crystal plasticity

A rate-independent single-crystal plasticity model developed by Anand and Kothari [28] is used for modeling the material response of the bulk grains and melt pools. Crystal plasticity let us account for orientation dependent slip in grains that is a key feature of SLM metal structures. In crystal plasticity theory, the plastic deformation in single crystals is supposed to take place through a simple shear on a specific set of slip planes. The combination of a slip plane (named by its normal n^α) and a slip direction (denoted by m^α) is called a slip system (α). The constitutive equations relate the deformation gradient F, which can be decomposed into elastic and plastic parts as Eq. (5), the slip resistances $s^\alpha > 0$, and the Cauchy stress T.

$$F = F^e F^p \tag{5}$$

To characterize small elastic strains, the Green elastic strain measure (Eq. (6)) is defined on the relaxed configurations (plastically deformed, unstressed configuration). The conjugate stress measure is then assessed by using Eq. (7), and the stress-strain relationship is given by Eq. (8).

$$\overline{E}^e = \frac{1}{2}\left(F^{eT}F^e - I\right) \tag{6}$$

$$\overline{T} = \det F^e \left(F^e\right)^{-1} T \left(F^e\right)^{-T} \tag{7}$$

$$\overline{T} = C\left[\overline{E}^e\right] \tag{8}$$

where C is the fourth-order elasticity tensor.

The evaluation of the plastic flow (L^p) is given by:

$$L^p = \dot{F}^p \left(F^p\right)^{-1} = \sum_\alpha \dot{\gamma}^\alpha S_0^\alpha \; sign(\tau^\alpha) \tag{9}$$

Where $S_0^\alpha = m^\alpha \otimes n^\alpha$ is the Schmid tensor and $\dot{\gamma}^\alpha$ is the plastic shearing rate on the α^{th} slip system. The resolved shear stress τ^α on the α^{th} slip system is calculated by:

$$\tau^\alpha = \overline{T}.S_0^\alpha \tag{10}$$

Table 4
The calibrated elastic and plastic material constants used to define the properties of grain structures.

Constant	C_{11} (GPa)	C_{12} (GPa)	C_{44} (GPa)	s_0 (MPa)	h_0	q	a
Value	107.10	46.80	70.10	195.0	120	1.4	1.5

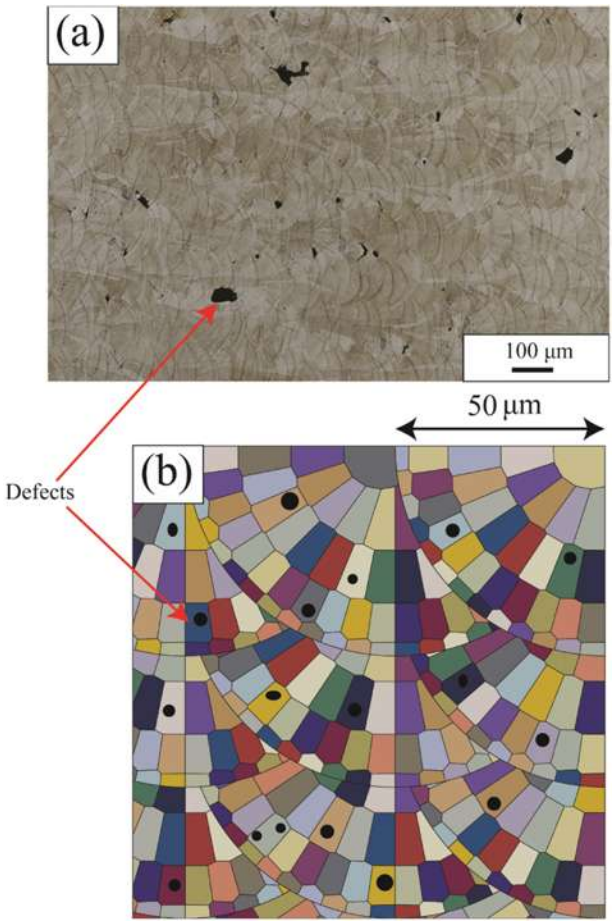

Fig. 9. (a) Optical microscopy image of SLM 316L stainless steel showing the presence of processing inclusions. (b) A schematic representation of the RVE model including the processing defects such as unmelted regions and porosities. The defects are randomly distributed in RVE model.

The resolved shear stress τ^{α} on the active slip system ($\dot{\gamma}^{\alpha}>0$), reaches a critical value s^{α} on the systems where the slip occurs. However, the resolved shear stress τ^{α} does not exceed s^{α} on the inactive slip systems with $\dot{\gamma}^{\alpha}=0$. The hardening law for the slip resistance s^{α} is given as:

$$\dot{s}^{\alpha}(t)=\sum_{\beta}h^{\alpha\beta}\dot{\gamma}^{\beta},s^{\alpha},(0)=s_0^{\alpha} \tag{11}$$

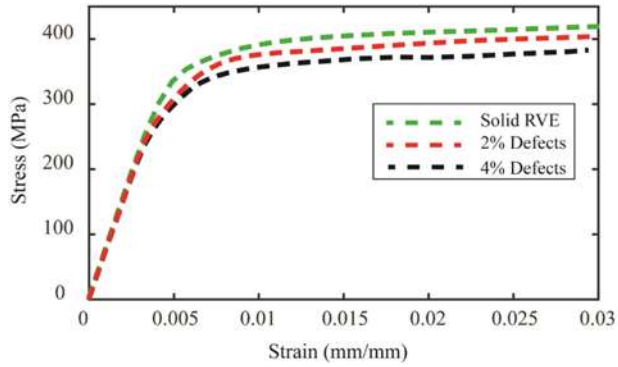

Fig. 10. Stress (along y-axis)-strain (along y-axis) response of the solid RVE compared to the RVE with 2 volume percentage and 4 volume percentage of defects. The defects show a significant role on the mechanical performance of SLM products.

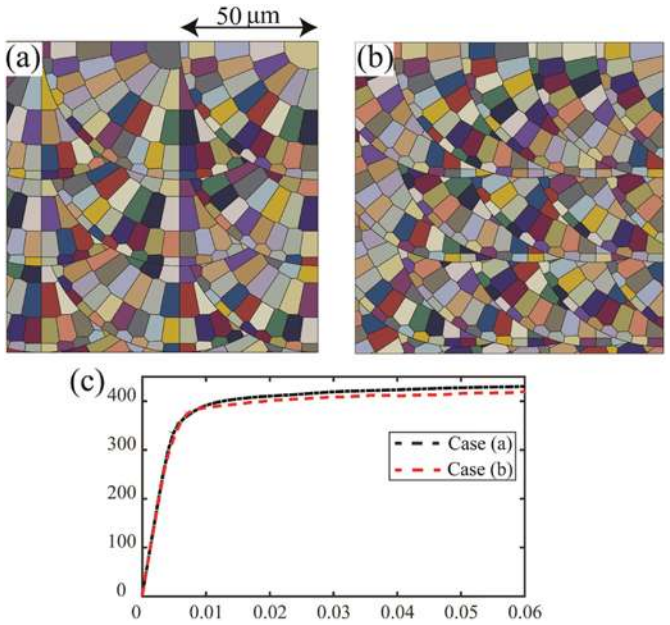

Fig. 11. (a) The RVE size with 50% overlapping of the melt pools, (b) the RVE size with 75% overlapping of the melt pools, (c) the stress (along y-axis)-strain (along y-axis) response of both cases show decreasing the yield strength and the level of plastic flow by increasing decreasing the hatch space.

The slip system hardening model is taken as:

$$h^{\alpha\beta}=\left[q+(1-q)\delta^{\alpha\beta}\right]h^{\beta}\ (\text{no sum on }\beta) \tag{12}$$

where h^{β} is a single slip hardening rate, $\delta^{\alpha\beta}$ is the Kronecker delta function, and q is the latent-hardening ratio. For the single-slip hardening rate, a specific form described in Eq. (13) is adopted.

$$h^{\beta}=h_o\left(1-\frac{s^{\beta}}{s_s}\right)^{\alpha} \tag{13}$$

where h_o, a, and s_s are slip hardening parameters.

The described, crystal plasticity constitutive model is previously implemented into a user-defined material subroutine (VUMAT) by Sundararaghavan et al. [29]. This VUMAT will be employed in this project properly. For simplification, the same material properties will be applied to all melt pools/grains boundaries.

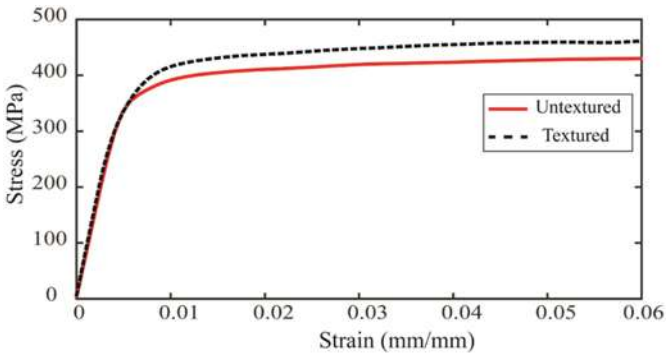

Fig. 12. The Stress (along y-axis)-strain (along y-axis) response of textured and untextured RVE models. The results indicate the capability of the model on predicting the effect of crystal orientations of grains on mechanical properties of SLM products.

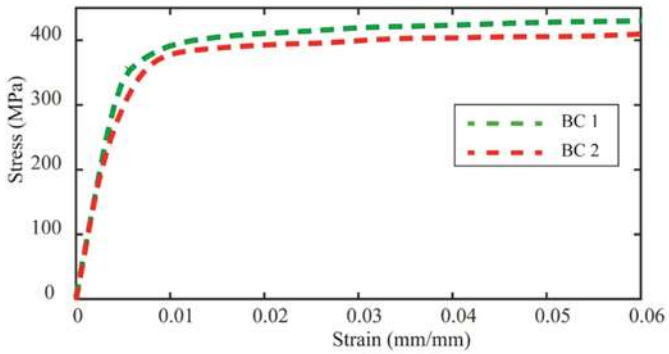

Fig. 13. The Stress (along y-axis)-strain (along y-axis) response of RVEs under two different loading conditions. BC1 shows superior mechanical properties because the direction of grains (columnar grains) is in the same direction of the mechanical loading.

5. Results and discussion

5.1. The role of RVE size

An important parameter which may influence the overall mechanical behavior is the RVE size. To adequately describe the mechanical properties of a polycrystalline material made by SLM, the size of the RVE needs to be large enough to contain a sufficient number of grains and melt pools. However, the computational costs will increase by increasing the size of the RVE. To select an appropriate RVE size, several volume elements (VE) are created and tested for convergence of the obtained results in terms of yield stress. Table 3 and Fig. 5 demonstrate the geometrical features of each VE and the schematics of some of the studied RVEs, respectively. As shown in Fig. 6, convergence is achieved for the prediction of VE 4, VE 5, and VE 6. The results of the RVEs larger than 210 μm (VE 4) converge to a specific value. Therefore, the acceptable size of the RVE is considered as a minimum of 275 μm (RVE 5) in this study. Fig. 7(a) illustrates RVE 5 which includes 11 melt pools and 319 grains. The corresponding grain surface area distribution and aspect ratio of grains are shown in Fig. 7(b) and (c), respectively. It worth noting that the crystal plasticity parameters used in this section are chosen arbitrarily, and as a result of it, the simulation results shown in Fig. 6 is not in agreement with experimental data in Fig. 2. The calibration of the modeling based on the experimental data is conducted and explained in the fowling section (Section 5.2).

5.2. Determination of crystal plasticity model parameters

The crystal-plasticity model is calibrated by simultaneously fitting the stress-strain response obtained from uniaxial tension tests described in Section 2. Since the experimental uniaxial tensile test is used for characterization, the same procedure is followed in simulation to mimic the loading conditions. Prior to fitting process, some material constants are estimated from the literature. For instance, a series of the model parameters are available for 316L stainless steel made by conventional techniques in [30], which serves as a general guideline on the initial estimations. Also, it is known that some of the model parameters have specific influence on the stress-strain response, e.g. s_0 parameter mainly influences the level of yield strength. Following each step, the resulting stress values at each strain are compared with the equivalent experimental data and the magnitude of the difference is considered in an error function. Optimization is performed until the error is minimized.

In Fig. 8, the stress-strain curves obtained from the fitting procedure are compared against the corresponding experimental data for a uniaxial tension test on SLM 316L stainless steel. To reduce the simulation cost, the level of strain in this plot (and the all the following simulation stress-strain plots in this study) is not similar to what experimentally reported in Fig. 2. It can be found from Fig. 8 that the model simulations agree well with data in terms of the elastic response of the material and its flow stress. The calibrated material constants are reported in Table 4. The same constants are used for several simulations presented in this paper.

Table 5
Boundary conditions applied to the RVE model (a × a × thickness). $\bar{v}_1$ is displacement of the top and bottom faces upon loading on the right.

Model face	Boundary condition
Top (y = a)	$v = \bar{v}_1$; $t_1 = t_3 = 0$
Bottom (y = 0)	$v = -\bar{v}_1$; $t_1 = t_3 = 0$
Left (x = 0)	$u = 0$; $t_2 = t_3 = 0$
Right (x = a)	u = displacement; $t_2 = t_3 = 0$

5.3. Investigation of effective parameters on mechanical properties of SLM components

Several different case studies are presented in this section for analyzing various aspects of the mechanical response of polycrystalline 316L stainless steel made by SLM. In Section 5.3.1 the role of defects (porosities, and unmelted regions) on mechanical properties of SLM components is investigated. The effect of changing hatch space, the crystallographic orientation of grains, and the mechanical loading directions on functional behavior of polycrystalline SLM samples are discussed in the following sections. Conducting more experimental works on SLM parts made by different processing conditions and comparing them with the potentials of the model explained in this section is very crucial and it will be the subject of a future communication by the authors.

5.3.1. The effect of processing defects

Defect formation is a common issue in selective laser melting (SLM) process. High energy density of the laser beam during SLM process results in the creation of high recoil pressure above the melt pool. The pressure caused a portion of the molten material (called spatter particles) to be ejected from the molten zone and fall down to the solidified layer. As the next powder layer is coated, the spatter particles remain as a non-melted region in the parts [31]. Metallurgical pores may also be induced during SLM process at slow laser scanning speeds from gases trapped within the melt pool or arisen from the powder during consolidation [32]. Moreover, keyhole pores may cause from keyhole instability due to rapid solidification of the metal without the complete filling of gaps with molten metal [33]. The described defects are found to have a significant detrimental effect on mechanical properties of SLM components [31,34,35]. Fig. 9(a) shows the presence of described processing defects in SLM 316 L stainless steel samples. To take them into account, randomly distributed inclusion are created in the RVE as shown in Fig. 9(b). Two different levels of porosity, (2% and 4%) are produced and the obtained results are compared with the non-porous model as shown in Fig. 10. The selected levels of porosities are in the range of currently reported defect percentages in the SLM products. The model clearly predicts the significant loss in mechanical strength and the level of plastic flow of SLM part by increasing the level of porosity.

5.3.2. The role of hatch space

The distance between two consecutive parallel laser tracks called Hatch Space (HS) is one of the required parameters needed to be specified during SLM process. HS controls the percentage of overlapping of two successive melt pools in one layer. To investigate the effect of HS on mechanical properties of SLM alloys, RVEs with 50% and 75% overlaps are made as shown in Fig. 11(a) and (b), respectively. The selected overlaps percentages are in agreement with the reported range using in SLM manufacturing process. Stress-strain responses, exhibited in Fig. 11(c), indicate decreasing the amount of HS results in decreasing the yield

stress and level of plastic flow. However, a number of the differences between two cases is less than what has been observed in experimental studies. It is because the effects of the interface mechanics of melt pool boundaries and remelting on microstructural features are not taken into account in the current version of models, and will be the subject of a future report by the authors. The existing difference is mostly due to decreasing the number of columnar grains by increasing the overlapping of two following melt pool.

5.3.3. The role of texture

It has been shown that a controllable texture can be achieved by changing the manufacturing process parameters such as hatch space and layer thickness [22]. In this section, the potential of the model in capturing the effect of texture on the mechanical response of polycrystalline SLM 316L stainless is illustrated. Two different distribution of crystal orientations in the grains is considered. For modeling the untextured material, a random orientation is applied to each grain. For modeling the textured material, a textured orientation is assigned to each grain such that the [111] directions of the lattice are distributed highly aligned along the x-direction (see Fig. 4) with a small deviation based on a Gaussian distribution, while the [001] directions are randomly distributed [36]. The results (Fig. 12) reveal that mechanical properties including the yield stress and the level of the plastic flow of the textured SLM materials are superior compared to the untextured ones. This understanding is in good agreement with the experimental results reported in [22].

5.3.4. Mechanical loading direction effect

The capability of the model in predicting the effect of loading direction on the mechanical behavior of SLM parts is studied in this section. The uniaxial tension test for the polycrystalline model shown in Fig. 4 by applying the boundary condition described in Table 2 (BC1) and Table 5 (BC2) are compared. In this table,t_1, t_2, and t_3 represent the tractions in X,Y, and Z directions, respectively. The uniaxial stress-strain curves presented in Fig. 13 show the yield stress and plastic flow level for the model with BC1 are higher than the model with BC2. The possible reason behind this finding is the columnar grains in a model with BC1 are in the same direction of the loading direction. Consequently, the material shows higher yield strength in longitude orientation as compared to the transference orientation. Similar understanding on anisotropy in mechanical properties of SLM 316L stainless steel has been reported in [18].

6. Summary and conclusion

A novel technique is developed to simulate the geometrical features of metallic parts made by SLM technique. As observed experimentally, columnar grains, equiaxial grains, and melting pools are generated to accurately model the microstructures of SLM components. Crystal plasticity constitutive equations are implemented into the finite element model to simulate the mechanical properties of grains. Proper size of representative volume element which can objectively reflect the macroscopic features of SLM components is determined. Crystal plasticity material constants are assessed based on uniaxial tension test on polycrystalline SLM 316L stainless steel. The capability of the developed model in capturing the effect of processing defects such as porosity and unmelted regions are studied. Moreover, the roles of crystallographic orientations of grains, the direction of applied mechanical loading, and the distance between two consecutive parallel laser tracks (Hatch Space) on mechanical properties of polycrystalline SLM parts are investigated. The good agreement between the model results and the reported experimental data confirms the accuracy of the developed computational model. Consequently, the potential contribution of this research to the field is developing a comprehensive computational model for accurately predicting the mechanical response of SLM processed materials, considering the geometrical features of both the grains and melt pools explicitly. Future communications by the authors will study the fracture and fatigue mechanics of the current developed model to make the model more comprehensive.

Acknowledgment

The authors would like to acknowledge SLM Solutions Inc. for helping the authors to conduct the experiments. The authors are also grateful for help generously provided by Dr. Christian Heinrich during determination of crystal plasticity model parameters.

References

[1] B. Berman, 3-D printing: the new industrial revolution, Bus. Horiz. 55 (2) (2012) 155–162.
[2] N. Yang, Y. Tian, D. Zhang, Novel real function based method to construct heterogeneous porous scaffolds and additive manufacturing for use in medical engineering, Med. Eng. Phys. 37 (11) (2015) 1037–1046.
[3] M. Taheri Andani, C. Haberland, J.M. Walker, M. Karamooz, A. Sadi Turabi, S. Saedi, R. Rahmanian, H. Karaca, D. Dean, M. Kadkhodaei, Achieving biocompatible stiffness in NiTi through additive manufacturing, J. Intell. Mater. Syst. Struct. 27 (19) (2016) 2661–2671.
[4] M.M. Francois, A. Sun, W.E. King, N.J. Henson, D. Tourret, C.A. Bronkhorst, N.N. Carlson, C.K. Newman, T. Haut, J. Bakosi, Modeling of additive manufacturing processes for metals: challenges and opportunities, Curr. Opinion Solid State Mater. Sci. (2017).
[5] A. Ahmadi, R. Mirzaeifar, N.S. Moghaddam, A.S. Turabi, H.E. Karaca, M. Elahinia, Effect of manufacturing parameters on mechanical properties of 316L stainless steel parts fabricated by selective laser melting: a computational framework, Mater. Des. 112 (2016) 328–338.
[6] A. Ahmadi, N.S. Moghaddam, M. Elahinia, H.E. Karaca, R. Mirzaeifar, Finite element modeling of selective laser melting 316l stainless steel parts for evaluating the mechanical properties, Proceedings of the ASME 2016 11th International Manufacturing Science and Engineering Conference, Blacksburg, VA, USA, 2016.
[7] C. Yan, L. Hao, A. Hussein, P. Young, D. Raymont, Advanced lightweight 316L stainless steel cellular lattice structures fabricated via selective laser melting, Mater. Des. 55 (2014) 533–541.
[8] J. Sun, Y. Yang, D. Wang, Mechanical properties of a Ti6Al4V porous structure produced by selective laser melting, Mater. Des. 49 (2013) 545–552.
[9] M. Karamooz-Ravari, S.N. Esfahani, M.T. Andani, M. Kadkhodaei, A. Ghaei, H. Karaca, M. Elahinia, On the effects of geometry, defects, and material asymmetry on the mechanical response of shape memory alloy cellular lattice structures, Smart Mater. Struct. 25 (2) (2016) 025008.
[10] A. Ahmadi, A Micromechanical-based Computational Framework for Modeling the Mechanical Properties of the Metallic Parts Fabricated by Selective Laser Melting, 2016.
[11] A. Foroozmehr, M. Badrossamay, E. Foroozmehr, Finite element simulation of selective laser melting process considering optical penetration depth of laser in powder bed, Mater. Des. 89 (2016) 255–263.
[12] S.A. Khairallah, A.T. Anderson, A. Rubenchik, W.E. King, Laser powder-bed fusion additive manufacturing: physics of complex melt flow and formation mechanisms of pores, spatter, and denudation zones, Acta Mater. 108 (2016) 36–45.
[13] C. Panwisawas, C. Qiu, M.J. Anderson, Y. Sovani, R.P. Turner, M.M. Attallah, J.W. Brooks, H.C. Basoalto, Mesoscale modelling of selective laser melting: thermal fluid dynamics and microstructural evolution, Comput. Mater. Sci. 126 (2017) 479–490.
[14] R. Acharya, J.A. Sharon, A. Staroselsky, Prediction of microstructure in laser powder bed fusion process, Acta Mater. 124 (2017) 360–371.
[15] P. Nie, O. Ojo, Z. Li, Numerical modeling of microstructure evolution during laser additive manufacturing of a nickel-based superalloy, Acta Mater. 77 (2014) 85–95.
[16] A. Standard, E8, standard test methods for tension testing of metallic materials, Annual book of ASTM Standards, 3, 2004, pp. 57–72.
[17] M.T. Andani, C. Haberland, J. Walker, M. Elahinia, An investigation of effective process parameters on phase transformation temperature of nitinol manufactured by selective laser melting, ASME 2014 Conference on Smart Materials, Adaptive Structures and Intelligent Systems, American Society of Mechanical Engineers, 2014 (pp. V001T01A026–V001T01A026).
[18] J. Suryawanshi, K. Prashanth, U. Ramamurty, Mechanical behavior of selective laser melted 316L stainless steel, Mater. Sci. Eng. A 696 (2017) 113–121.
[19] F. Fritzen, T. Böhlke, E. Schnack, Periodic three-dimensional mesh generation for crystalline aggregates based on Voronoi tessellations, Comput. Mech. 43 (5) (2009) 701–713.
[20] B. Boots, The arrangement of cells in "random" networks, Metallography 15 (1) (1982) 53–62.
[21] C. Rycroft, Voro++: A Three-dimensional Voronoi Cell Library in C++, 2009.
[22] L. Thijs, K. Kempen, J.-P. Kruth, J. Van Humbeeck, Fine-structured aluminium products with controllable texture by selective laser melting of pre-alloyed $AlSi_{10}Mg$ powder, Acta Mater. 61 (5) (2013) 1809–1819.
[23] W. Shifeng, L. Shuai, W. Qingsong, C. Yan, Z. Sheng, S. Yusheng, Effect of molten pool boundaries on the mechanical properties of selective laser melting parts, J. Mater. Process. Technol. 214 (11) (2014) 2660–2667.
[24] K. Saeidi, X. Gao, Y. Zhong, Z.J. Shen, Hardened austenite steel with columnar subgrain structure formed by laser melting, Mater. Sci. Eng. A 625 (2015) 221–229.
[25] N.H. Abid, R.K.A. Al-Rub, A.N. Palazotto, Micromechanical finite element analysis of the effects of martensite morphology on the overall mechanical behavior of dual phase steel, Int. J. Solids Struct. 104 (2017) 8–24.

[26] B. Wu, N. Vajragupta, J. Lian, U. Hangen, P. Wechsuwanmanee, S. Münstermann, Prediction of plasticity and damage initiation behaviour of C45E+ N steel by micromechanical modelling, Mater. Des. 121 (2017) 154–166.
[27] H. Shen, L.C. Brinson, A numerical investigation of the effect of boundary conditions and representative volume element size for porous titanium, J. Mech. Mater. Struct. 1 (7) (2006) 1179–1204.
[28] L. Anand, M. Kothari, A computational procedure for rate-independent crystal plasticity, J. Mech. Phys. Solids 44 (4) (1996) 525–558.
[29] P.I.S.M.S.P. Center, PRISMS-plasticity, https://github.com/prisms-center/plasticity.
[30] I. Simonovski, K.-F. Nilsson, L. Cizelj, Material properties calibration for 316 L steel using polycrystalline model, The 13th International Conference on Nuclear Engineering Abstracts, 2005.
[31] M.T. Andani, R. Dehghani, M.R. Karamooz-Ravari, R. Mirzaeifar, J. Ni, Spatter formation in selective laser melting process using multi-laser technology, Mater. Des. (2017).
[32] N.B. Dahotre, S. Harimkar, Laser Fabrication and Machining of Materials, Springer Science & Business Media, 2008.
[33] N.T. Aboulkhair, N.M. Everitt, I. Ashcroft, C. Tuck, Reducing porosity in $AlSi_{10}Mg$ parts processed by selective laser melting, Addit. Manuf. 1 (2014) 77–86.
[34] B. Zhang, Y. Li, Q. Bai, Defect formation mechanisms in selective laser melting: a review, Chin. J. Mech. Eng. (2017) 1–13.
[35] M. Karamooz-Ravari, M. Kadkhodaei, A computationally efficient modeling approach for predicting mechanical behavior of cellular lattice structures, J. Mater. Eng. Perform. 24 (1) (2015) 245–252.
[36] R. Mirzaeifar, R. DesRoches, A. Yavari, K. Gall, A micromechanical analysis of the coupled thermomechanical superelastic response of textured and untextured polycrystalline NiTi shape memory alloys, Acta Mater. 61 (12) (2013) 4542–4558.